Nanostructures in structured light: Photoinduced spin and orbital electron dynamics

Jonas Wätzel,[1] E. Y. Sherman,[2] and Jamal Berakdar[1]

[1]*Institute for Physics, Martin-Luther-University Halle-Wittenberg, 06099 Halle, Germany*

[2]*Department of Physical Chemistry, University of the Basque Country UPV-EHU, 48940 Bilbao, Spain and IKERBASQUE, Basque Foundation for Science, Bilbao, Spain*

(Received 4 March 2020; accepted 15 May 2020; published 3 June 2020)

We study the coupled spin and orbital dynamics of electrons in one- and two-dimensional quantum dots driven by few cycle pulses of polarization-structured terahertz vector fields. Emphasis is put on the use of radially and azimuthally polarized, cylindrical vector beams for spin-flip processes caused by transitions between electronic states characterized by spin-position entanglement and corresponding injection of spin currents. We demonstrated how different topologies of the beams result in different selection rules and corresponding spin and position dynamics. These results point to new possibilities for spatiotemporal control of the coupled spin and orbital electron dynamics via polarization shaping of the driving electromagnetic pulse.

DOI: 10.1103/PhysRevB.101.235304

I. INTRODUCTION

Many relativistic effects in the dynamics of itinerant carriers in solids can be concisely described with various spin-orbit coupling Hamiltonians. These Hamiltonians can be expressed in terms of products of powers of momentum and spin operators corresponding to the symmetry of the crystal [1]. Experimentally, current techniques for fabricating nanostructures allow designing, to a large degree, the desired spin-orbit coupling Hamiltonians [2]. One of the most exciting phenomena resulting from the spin-orbit coupling is the ability to manipulate the spin state with electric fields [3–5]. The basic example of this manipulation is the electric dipole spin resonance for itinerant and localized electrons, where a linearly polarized electric field produces Rabi-like spin rotation. Here, even at a rather weak spin-orbit coupling, the effect of the electric field on the spin dynamics can be much stronger than the effect of the magnetic field. Other forms of the electric dipole spin resonance are related to driven electron motion in a slanting magnetic field [6] and to the hyperfine coupling in quantum dots [7]. Another example of current interest is related to the reciprocal use of spin and charge currents and densities to produce spin polarization and spin currents by a static electric field [8].

Further opportunities for spin manipulation in semiconductors rely on quantum-mechanical optical processes [9,10], including stimulated Raman scattering [11]. The efficiency of the optical techniques strongly depends on the details of the incident optical fields. In these studies, mostly linear and circular polarizations have been explored. As recent advantages in nanotechnologies permitted modification of the spin-orbit coupling, recent progress in optical technologies permitted design of structured electromagnetic fields (see, e.g. Refs. [12–15]), thus posing problems regarding both the efficiency and novel features of spin dynamics induced by optical fields in novel solid-state–based nanostructures.

For example, cylindrical vector beams (CVBs) [14–17] can show efficient manipulation of the ratio of electric and magnetic fields which may have consequences on the optical EM-driven spin dynamics in spin-active quantum structures. The charge dynamics driven by radially and azimuthally polarized vector beams (RVB and AVB, respectively) was recently studied in quantum rings and atoms [18]. The RVB initiates a radial charge breathing as a result of quadrupole transitions, while the irradiation with an AVB results in the emergence of a time-dependent Aharonov-Bohm effect.

The scope of the paper is the extension of the theoretical investigation to the spin dynamics in a spin-active quantum structure based on the analysis of the entangled spin-position motion leading to spin-flip processes and spin current injection. It will be demonstrated that the RVB acts only on the charge position through electrically dominated light-matter interaction. Due to symmetry, spin-flip transitions and spin dynamics cannot be initiated. In contrast, the AVB is characterized by a strong longitudinal magnetic component which can drive spin currents and spin-flip transitions. Thus, changing the topology of the incident light wave has drastic consequences for the spin and charge dynamics.

II. THEORETICAL MODEL

A. Stationary electron states

The Hamiltonian of an electron confined to a quantum structure in the presence of an external static magnetic field is given by

$$\hat{H}_0 = \frac{1}{2m^*}(\boldsymbol{p} - e\boldsymbol{A}_{\rm st})^2 + U_\perp(x,y) + U_\parallel(z) + \frac{\alpha_R}{\hbar}[\hat{\boldsymbol{\sigma}} \times \boldsymbol{p}]_z + \frac{1}{2}g^*\mu_B B \cdot \hat{\boldsymbol{\sigma}}, \quad (1)$$

where m^* is the effective mass, $\boldsymbol{p}$ is the momentum operator, e is the electron charge, and we assume the speed of light $c \equiv 1$. Further we introduce the spatially dependent potentials $U_\perp(x,y)$ and $U_\parallel(z)$. In the following we assume that $U_\parallel(z)$ is strong enough that only the lowest subband is occupied

(also during the light-induced dynamics), mapping our system effectively into a two-dimensional problem. The parameter α_R is the spin-orbit coupling strength, while $\hat{\boldsymbol{\sigma}}$ denotes the vector of Pauli matrices. Note that $[\,]_z$ is a short notation for the z component of the vector $[\hat{\boldsymbol{\sigma}} \times \boldsymbol{p}]$. The vector potential describes the external uniform magnetic field via $\boldsymbol{B} = \nabla \times \boldsymbol{A}_{\rm st}$. Here we used the Landau gauge, i.e., $A(\boldsymbol{r}) = x\boldsymbol{B}_\parallel \hat{\epsilon}_y + y\boldsymbol{B}_\perp \hat{\epsilon}_z$, which yields $\boldsymbol{B} = \boldsymbol{B}_\perp \hat{\epsilon}_x + \boldsymbol{B}_\parallel \hat{\epsilon}_z$.

To compute the ground-state electronic spectrum we transform $\hat{H}_0$ into matrix representation in the basis of eigenfunctions $|\uparrow\rangle, |\downarrow\rangle$ of the Pauli matrix σ_z. The diagonal matrix elements read

$$H_{nn} = -\frac{\hbar^2}{2m^*}\nabla_\perp^2 + \frac{ie\hbar}{m^*}\boldsymbol{A}_{\rm st}\cdot\nabla_\perp + \frac{e^2}{2m^*}\boldsymbol{A}_{\rm st}^2 + U_\perp(x,y) - (-1)^n \frac{1}{2} g^* \mu_B B_\parallel, \tag{2}$$

with $n = 1, 2$, while the nondiagonal elements are

$$H_{nm} = \pm\alpha_R(\partial_x \pm i\partial_y) + \tfrac{1}{2} g^* \mu_B B_\perp. \tag{3}$$

The diagonalization leads to our basis states with the wave functions $\Psi_n(\boldsymbol{r}) = \varphi_n^\uparrow(\boldsymbol{r})|\uparrow\rangle + \varphi_n^\downarrow(\boldsymbol{r})|\downarrow\rangle$ and the corresponding energies ε_n. Further, for a qualitative analysis, it is convenient to characterize the electron states by the sign of the expectation value $\langle\Psi_n|\sigma_z|\Psi_n\rangle$. Note that in the presence of spin-orbit coupling, $|\langle\Psi_n|\sigma_z|\Psi_n\rangle| < 1$.

B. Vector beam-matter interaction

The time-dependent Hamiltonian $\hat{H}_{\rm int}(t)$ characterizes the light-matter interaction between the quantum structure confined electrons and the external spatially inhomogeneous laser field. In its most general form, it is given by the minimal coupling scheme

$$\begin{aligned} \hat{H}_{\rm int}(t) &= \hat{H}_1(t) + \hat{H}_2(t) + \hat{H}_3(t), \\ \hat{H}_1(t) &= \frac{ie\hbar}{2m^*}[\nabla\cdot\boldsymbol{A}(\boldsymbol{r},t) + 2\boldsymbol{A}(\boldsymbol{r},t)\cdot\nabla] - e\Phi(\boldsymbol{r},t), \\ \hat{H}_2(t) &= \frac{e^2}{2m^*}\boldsymbol{A}^2(\boldsymbol{r},t), \\ \hat{H}_3(t) &= -\frac{e\alpha}{\hbar}[\hat{\boldsymbol{\sigma}}\times\boldsymbol{A}(\boldsymbol{r},t)]_z, \end{aligned} \tag{4}$$

where $\boldsymbol{A}(\boldsymbol{r},t)$ and $\Phi(\boldsymbol{r},t)$ are the space and time-dependent vector and scalar potentials, respectively.

Cylindrical vector beams (CVBs) are characterized by their exotic polarization states and can be represented mathematically by a superposition of optical vortices [17,19]. Since the dimension (submicrometer scale) of our quantum structure is much smaller than the typical THz wavelength of the pulses, the quantum dot is well localized near the optical axis. Hence, for the radial distribution, it is not essential which exact mathematical mode (Bessel, Laguerre-Gaussian, etc.) is used for the description. In all cases, the near-optical axis transversal electric field amplitude is increasing linearly with the axial distance to it, i.e., $E_\perp \sim \rho$, where $\rho = \sqrt{x^2+y^2}$. In the following calculations, we use Bessel modes since they represent solenoidal vector fields, i.e., $\nabla\cdot\boldsymbol{A}_{\rm i} = 0$ ($i =$ RVB, AVB) [13]. The radial polarized vector beam (RVB) is described by the following vector potential in cylindrical coordinates $\boldsymbol{r} = \{\rho, \varphi, z\}$:

$$\boldsymbol{A}_{\rm RVB}(\boldsymbol{r},t) = A_0\Omega(t)\Big[-J_1(q_\perp\rho)\cos(q_\parallel z - \omega t)\hat{\epsilon}_\rho + \frac{q_\perp}{q_\parallel}J_0(q_\perp\rho)\sin(q_\parallel z - \omega t)\hat{\epsilon}_z\Big], \tag{5}$$

with the scalar potential $\Phi_{\rm RVB}(r,t) = 0$. The azimuthally polarized variant (AVB) is given by

$$\boldsymbol{A}_{\rm AVB}(\boldsymbol{r},t) = A_0\Omega(t)J_1(q_\perp\rho)\sin(q_\parallel z - \omega t)\hat{\epsilon}_\varphi, \tag{6}$$

and $\Phi_{\rm AVB}(r,t) = 0$. Here, we introduce the wave vector $q = \omega/c$ and its transversal (longitudinal) projection $q_\perp = q\sin\beta$ ($q_\parallel = q\cos\beta$), where β is the opening angle of the Bessel beam cone (typically below 10°) relative to the optical axis, which is identical to the z axis of the quantum structure. Further, the field amplitude is A_0 while the temporal envelope function reads explicitly $\Omega(t) = \cos[\pi t/T_p]^2$, with $t \in [-T_p/2, T_p/2]$, where the pulse length is given in optical cycles n_p, i.e., $T_p = 2\pi n_p/\omega$. For $n_p \to \infty$ we obtain a *continuous wave* pulse (purely harmonic perturbation). Since $\nabla\cdot A = 0$ in both cases, the scalar potential vanishes in the Lorenz gauge. Hence, electric and magnetic fields can be evaluated via $\boldsymbol{E}(\boldsymbol{r},t) = -\partial_t\boldsymbol{A}(\boldsymbol{r},t)$ and $\boldsymbol{B}(\boldsymbol{r},t) = \nabla\times\boldsymbol{A}(\boldsymbol{r},t)$.

From the formal definitions alone, it is impossible to estimate the impact of the space-dependent polarization state on the dynamics in a spin-active quantum structure. Hence, it is more convenient to introduce different gauge potentials by exploiting the gauge freedom [18,20]. A practical choice is given by electromagnetic potentials in the Poincaré form:

$$\begin{aligned} \boldsymbol{A}'(\boldsymbol{r},t) &= -\boldsymbol{r}\times\int_0^1 d\lambda\,\lambda\boldsymbol{B}(\lambda\boldsymbol{r},t), \\ \Phi'(\boldsymbol{r},t) &= -\boldsymbol{r}\cdot\int_0^1 d\lambda\,\boldsymbol{E}(\lambda\boldsymbol{r},t). \end{aligned} \tag{7}$$

They simplify the interaction Hamiltonian $\hat{H}_{\rm int}(t)$ to a high degree, as we see in the following steps. In the case of the RVB we find the potentials in the plane $z = 0$ and near the optical axis (see Appendix):

$$\begin{aligned} \boldsymbol{A}'_{\rm RVB}(\boldsymbol{r},t) &= \frac{q_\perp q^2}{6q_\parallel}A_0\rho^2\Omega(t)\sin(\omega t)\hat{\epsilon}_z, \\ \Phi'_{\rm RVB}(\boldsymbol{r},t) &= \frac{1}{4}eE_0q_\perp\rho^2\Omega(t)\sin(\omega t), \end{aligned} \tag{8}$$

with $E_0 = A_0\omega$. Interestingly, the gauge-transformed vector potential $\boldsymbol{A}'(\boldsymbol{r},t)$ points at the z direction, which means that after insertion in the interaction Hamiltonian in Eq. (4), it has no impact on the electron dynamics confined to the plane $z = 0$, since $[\boldsymbol{A}'(\boldsymbol{r},t)\times\hat{\boldsymbol{\sigma}}]_z \equiv 0$ and $\boldsymbol{A}(\boldsymbol{r},t)\cdot\nabla$ act out of plane. Physically, the interaction with the RVB acts only on the position of charge carrier via the electric scalar potential. Hence, due to the symmetry no spin dynamics can be initiated, which is in contrast to the conventional electric dipole spin resonance realization.

The same procedure on the AVB reveals the following electromagnetic potentials:

$$\begin{aligned} \boldsymbol{A}'_{\rm AVB}(\boldsymbol{r},t) &= -\tfrac{1}{2}q_\perp\boldsymbol{A}_0\rho\Omega(t)\sin(\omega t)\hat{\epsilon}_\varphi, \\ \Phi'_{\rm AVB}(\boldsymbol{r},t) &= 0 \quad (\boldsymbol{r}\cdot\hat{\epsilon}_\varphi \equiv 0). \end{aligned} \tag{9}$$

In strong contrast to the RVB, we have no electric coupling to the charge carries due to the vanishing scalar potential. However, we find an in-plane vector potential which couples to vector of Pauli matrices in Eq. (4). Moreover, $\boldsymbol{A}'(\boldsymbol{r},t)$ coincides with Eq. (6), representing the equivalence of the gauges [note that $J_1(q_\perp\rho)\simeq q_\perp\rho/2$ near the optical axis].

III. LIGHT–QUANTUM DOT INTERACTION

As an application, we model the quantum structure based on GaAs semiconductor material. The effective mass is $m^*=0.067m_e$ (m_e is the electron mass), while the Rashba constant α_R is given in units of $\alpha_0=1.5$ meV $\times\,10^{-6}$ cm. The electron Landé factor of GaAs is $g^*=-0.44$. The confinement potentials are modeled according to $U_\perp(x,y)=m^*(\Omega_x^2x^2+\Omega_y^2y^2)/2$. The ratio of Ω_y to Ω_x dedicates the preferred direction of the electron dynamics: for instance, $\Omega_y\gg\Omega_x$ effectively freezes the motion in y direction and generates a "nanowire-based"-like [21] one-dimensional (1D) quantum dot. In the following we fix the confinement strength in the x direction to $\hbar\Omega_x=10$ meV, with Ω_y being an adjustable parameter.

The time evolution of the corresponding density matrix is given by

$$\partial_t\rho_{nm}=-i\omega_{nm}\rho_{nm}-\frac{i}{\hbar}[\hat{H}_{\rm int}(t),\rho]_{nm},\\ -\gamma_{nm}\big(\rho_{nm}-\rho_{nm}^{\rm eq.}\big). \tag{10}$$

Here, $\rho_{nm}^{\rm eq.}$ is the unperturbed density matrix operator, and γ_{nm} is the phenomenological set of parameters describing the damping occurring in quantum dots mainly due to the electron-phonon interaction. It is assumed that γ_{nm} is a diagonal matrix and its elements are equal to the inverse of relaxation time $\tau_{\rm rel.}$. In what follows we neglect relaxation and assume $\gamma_{nm}=0$. In equilibrium $\rho_{nm}(t\to-\infty)=\rho_{nm}^{\rm eq.}=\delta_{n,1}\delta_{m,1}$, meaning the ground state is fully occupied. To reach convergence and accuracy to a high degree, we use a total number of $N=100$ electron states for the construction of the density matrix ρ_{nm}. Hence, any (realistic) multiphoton transitions are captured by the numerical propagation of the density matrix.

The analysis of the Poincaré gauge potentials revealed that the RVB would not initiate spin dynamics since it can be reduced to the action of an electromagnetic scalar potential in the case of a two-dimensional (2D) structure. Further, the interaction is a quadrupole-type, meaning we find transitions between quantum states characterized by both the same spin projection and spatial parity. An analysis of the electron spectrum shows that only the states $|\Psi_i\rangle$ with the same sign$\{\langle\Psi_i|\sigma_z|\Psi_i\rangle\}$ as the initial state can be occupied (which turns out to be a "selection rule" for first-order transitions). As a consequence, spin-flip transitions and the emergence of spin currents do not occur. Hence, in the following analysis we concentrate solely on the azimuthal vector beam, which is characterized by an in-plane Poincaré vector potential.

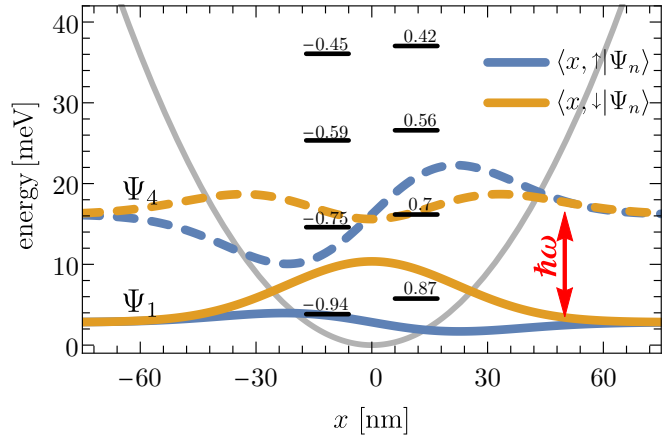

FIG. 1. Electron states in the 1D quantum dot. The spatial dependencies of the confinement potential $U_\perp(x,0)$ (gray), initial (blue) and target (orange) state wave functions are shown. Thick horizontal lines denote the energy levels of the lowest lying states. The number corresponds to expectation of the spin projection, i.e., $\langle\Psi_i|\sigma_z|\Psi_i\rangle$. The photon energy of the laser field is tuned to the quadrupole transition between the initial (1) and final state (4) where the spin-projected wave functions have the same parity.

A. AVB-driven 1D quantum dot

1. Spin-flip transition

A one-dimensional quantum dot can be produced [21] by a rapid increase of $U_\perp(x,y)$ with $|y|$, effectively freezing the electron dynamics in the y direction. The confinement has interesting consequences for the AVB-matter interaction: obviously, $\hat{\epsilon}_x\cdot\hat{\epsilon}_\varphi=0$ for $y=0$, i.e., $\boldsymbol{A}'_{\rm AVB}(\boldsymbol{r},t)\cdot\nabla=0$ so that $\hat{H}_1(t)=0$. Further, for moderate intensities, $\hat{H}_2(t)=e^2\boldsymbol{A}'^2(\boldsymbol{r},t)/2m^*$ can be safely ignored in the interpretation (it is nevertheless included in our numerical treatment but its impact is negligibly small). The physical meaning is that we can turn off the quadrupolar spin (projection) conserving interaction $\hat{H}_1(t)=0$ by exploiting the unique topology of the vector beam.

The remaining nonvanishing part is the spin (projection) nonconserving part given by $\hat{H}_3(t)=q_\perp eA_0\alpha_R\Omega(t)\sin(\omega t)\,x\sigma_x/2$. Here, we used again the localization of the quantum wire close to $\rho=0$, i.e., $J_1(q_\perp\rho)\simeq(1/2)q_\perp\rho$, while $\rho\hat{\epsilon}_\varphi=(-y,x)^{\rm T}$ [cf. Eq. (6)], where T denotes transposition. Hence, the combination of system and light field topologies causes the light-matter interaction to be directly proportional to the spin-orbit coupling constant α_R. As a consequence, for $\alpha_R\to0$ the whole interaction Hamiltonian $\hat{H}_{\rm int}$ is reduced to the ponderomotive potential given by $\hat{H}_2(t)$, which is negligibly small for the considered field intensities.

The first-order transitions in a spin-active 1D quantum dot can be understood by studying the electronic structure shown in the composite Fig. 1. In a finite magnetic field, $|\Psi_1\rangle$ ($\langle\sigma_z\rangle=-0.94$) represents the ground state where the spin-up (down) projection $\langle x,\downarrow(\uparrow)|\Psi_1\rangle$ is an odd (even) function. The only nonvanishing light-matter Hamiltonian $\hat{H}_3(t)$ allows only mixing between the spin projections. Further, $\hat{H}_3(t)$ is clearly an odd function so that the target spin projection of the final state has to be of opposite parity: in other words, an odd

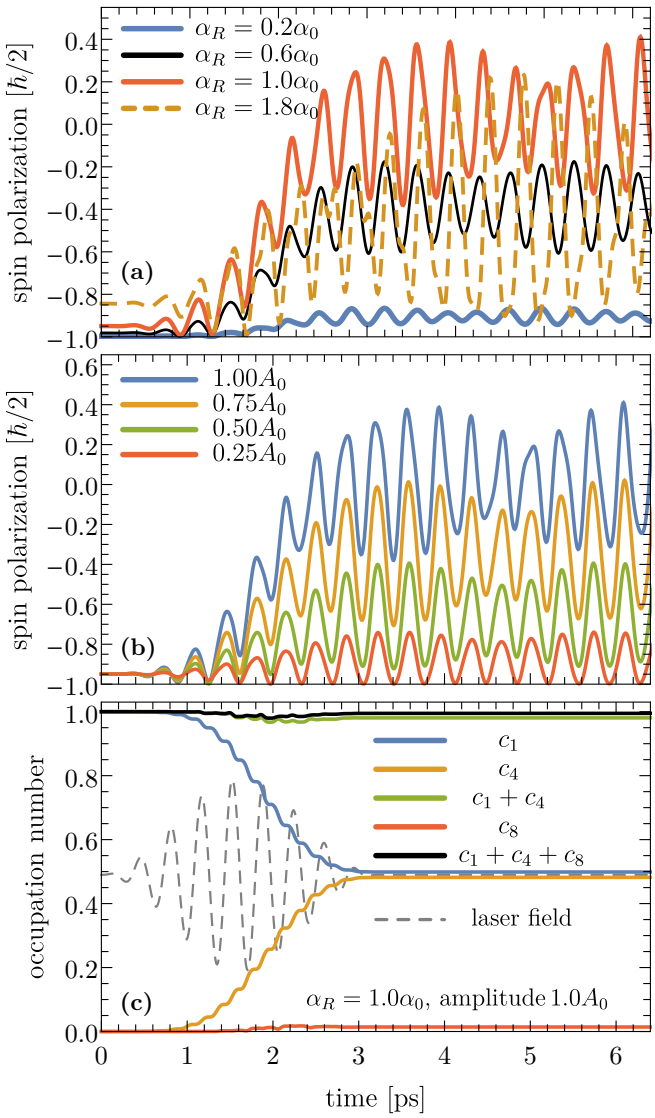

FIG. 2. Interaction of a quantum wire with an azimuthally polarized vector beam. (a) Time-dependent spin polarization for different SOC coupling strengths. Here $\alpha_0 = 1.5$ meV $\times 10^{-6}$ cm. (b) Time-dependent spin polarization for different field strengths at $\alpha_R = \alpha_0$. The basis value A_0 corresponds to the electric field of 700 kV/cm at the first maximum of the Bessel function $J_1(q_\perp \rho)$, which is located at $\rho_0 = 50$ μm. Such strong THz fields are feasible nowadays [22]. (c) Time-dependent occupation numbers of the states $|\Psi_1\rangle$ (ground state), $|\Psi_4\rangle$ (target state), and $|\Psi_8\rangle$ (accessible via multiphoton process). In addition, the sums $c_1 + c_4$ and $c_1 + c_4 + c_8$ are shown.

spin-up projection transitions into an even spin-down projection, and vice versa. Hence, the only possible (first-order) final state dedicated by the AVB-matter interaction is $|\Psi_4\rangle$, characterized by $\langle\Psi_4|\sigma_z|\Psi_4\rangle = 0.7$. Consequently, we identified a "selection rule" for AVB-driven first processes, i.e., $\mathrm{sgn}\{\langle\Psi_f|\sigma_z|\Psi_f\rangle\} = -\mathrm{sgn}\{\langle\Psi_i|\sigma_z|\Psi_i\rangle\}$, where f (i) denotes the final (initial) state.

As we already mentioned above, the striking feature of the AVB-matter interaction (at moderate intensity) is the direct proportionality with the spin-orbit coupling (SOC) constant α_R, since only $\hat{H}_3(t)$ is nonvanishing. In Fig. 2(a) we present the time variation of the spin polarization $\langle\Psi(t)|\sigma_z|\Psi(t)\rangle$ in dependence on the Rashba SOC coupling constant α_R. As expected, a larger α_R increases the transition probability $|\Psi_1\rangle \to |\Psi_4\rangle$, resulting in a change of the spin polarization of $|\Psi(t)\rangle$. Starting from $\langle\Psi(t)|\sigma_z|\Psi(t)\rangle = -0.94$ (mediated by the ground state $|\Psi_1\rangle$), the spin polarization increases during the interaction with light fields, since the final state $|\Psi_4\rangle$ is characterized by a positive $\langle\Psi_4|\sigma_z|\Psi_4\rangle$. For instance, at $\alpha_R = \alpha_0$ (red curve), we find a time-averaged (over oscillations corresponding to free propagation) $\langle\sigma_z\rangle$ of 0.05 directly after the vector beam light pulse is off. However, we find also a saturation, meaning that increasing α_R does not result necessarily in a higher spin polarization. As shown for $\alpha_R = 1.8\alpha_0$ (black curve), the value of $\langle\Psi(t)|\sigma_z|\Psi(t)\rangle$ immediately after the pulse is lower than for the case of the "maximal" effect at $\alpha_R = \alpha_0$. This can be explained by the stronger internal mixing between $|\uparrow\rangle$ and $|\downarrow\rangle$ projections of the electronic states with the consequence that $\langle\Psi_4|\sigma_z|\Psi_4\rangle$ decreases for a larger α_R. Hence, the maximal effect at $\alpha_R = \alpha_0$ characterizes a compromise between mixing of the spin projection within the eigenstates of $\hat{H}_0$ (decreases expectation value of σ_z) and the spin-flip transition probability, since both are determined by α_R.

Figure 2(b) shows the spin-flip process for different field amplitudes at a SOC strength $\alpha_R = \alpha_0$. Since we are still in the regime of the dominating single-photon processes, we find a proportionality between the spin flip (occupation of the target state 4) and the field amplitude. These results are assisted by panel (c), where we plotted explicitly the time dependence of the occupation numbers $c_i = |\langle\Psi_i|\Psi(t)\rangle|^2$ for $\alpha_R = \alpha_0$ and the field amplitude A_0: single-photon processes are characterizing mainly the spin-flip process, since the sum $c_1 + c_4$ is $\sim$0.9 after the end of the pulse. We also have a minor contribution of the state $|\Psi_8\rangle$ which is accessible only by multiphoton processes. Hence, a further increase of the amplitude or the SOC coupling strength α_R will lead to dominating multiphoton processes.

2. *Spin current injection*

Let us turn to the tensor operator for the spin current density given by [23]

$$\hat{\boldsymbol{j}}^s_{i,j} = \tfrac{1}{4}[|\boldsymbol{r}\rangle\langle\boldsymbol{r}|\hat{v}_i\hat{\boldsymbol{\sigma}}_j + (\hat{\boldsymbol{\sigma}}_j\hat{v}_i)^T|\boldsymbol{r}\rangle\langle\boldsymbol{r}|], \tag{11}$$

with the matrix elements

$$\left[j^s_{i,j}(\boldsymbol{r})\right]_{nm} = \tfrac{1}{4}[\langle n|\boldsymbol{r}\rangle\langle\boldsymbol{r}|\hat{v}_i\hat{\boldsymbol{\sigma}}_j|m\rangle + \langle n|(\hat{\boldsymbol{\sigma}}_j\hat{v}_i)^T|\boldsymbol{r}\rangle\langle\boldsymbol{r}|m\rangle], \tag{12}$$

where $\langle\boldsymbol{r}|m\rangle \equiv \Psi_m(\boldsymbol{r})$. Here, we introduce the velocity operator $\hat{\boldsymbol{v}} = (i/\hbar)[\hat{H}_0, \boldsymbol{r}]_-$. The volume-integrated spin current is given by

$$\left[I^s_{ij}\right]_{nm} = \int dr^3 \left[j^s_{i,j}(\boldsymbol{r})\right]_{nm}. \tag{13}$$

The expectation values of both operators are given by $j^s_{ij}(\boldsymbol{r},t) = \sum_{nm}[j^s_{i,j}(\boldsymbol{r})]_{nm}\rho_{mn}(t)$ and $I^s_{ij}(t) = \sum_{nm}[I^s_{ij}]_{nm}\rho_{mn}(t)$. Note that in our case, due to confinement only the dynamics in x direction is allowed, which reduces our spin current operators to $\langle\hat{I}^s_{x,i}\rangle(t)$, where the index $i = x, y, z$ indicates the Pauli matrix σ_i. In our case the velocity operator reduces to $\hat{v}_x = p_x/m^* + \alpha\sigma_y/\hbar$. As presented in Fig. 3(a), an analysis of the volume-integrated spin currents reveals

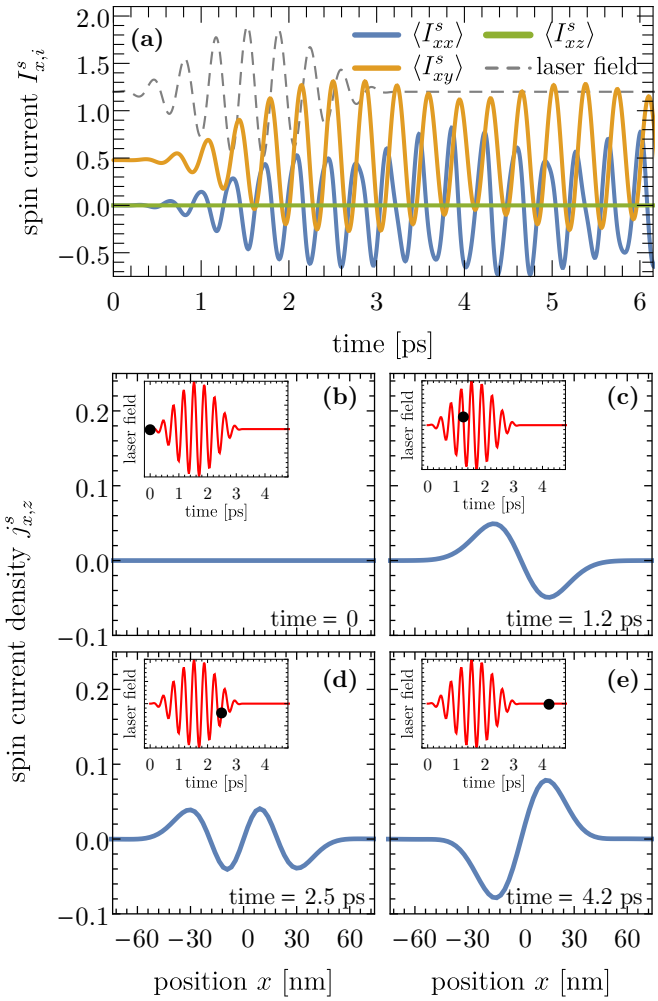

FIG. 3. Time evolution of the spin currents $I^s_{i,z}$ $(i = x, y, z)$ in panel (a) and spin current density $j^s_{x,z}$ in panels (b)–(e). The insets in (b)–(e) show the temporal profile of the incident laser field where the black dot represents the time moment of the shot (and the corresponding field strength). All curves belong to the parameters $\alpha_R = \alpha_0$ and A_0.

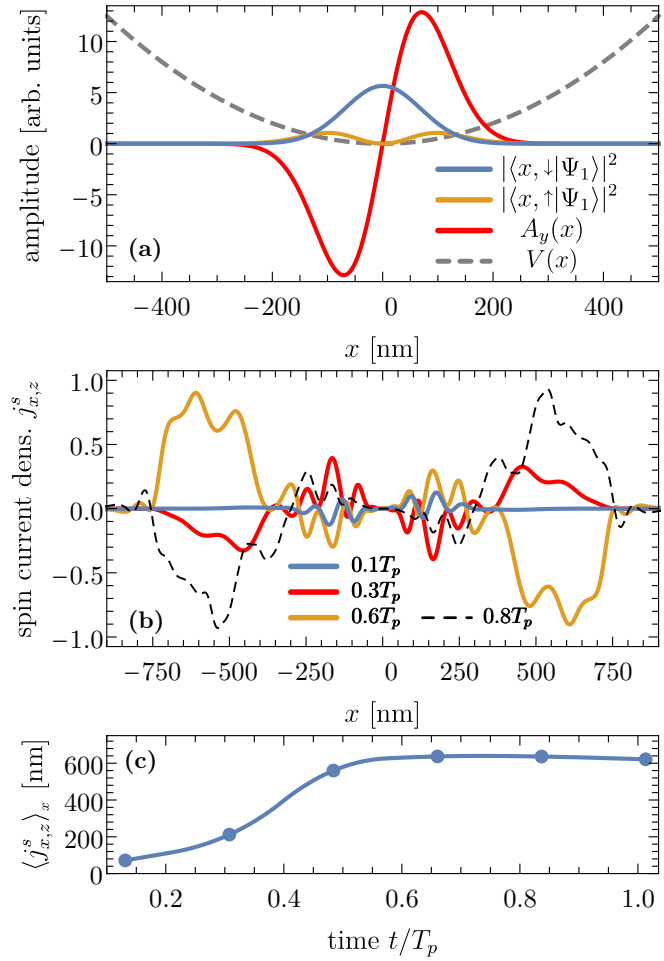

FIG. 4. Spin pumping with a local azimuthal vector beam. (a) Geometry of potential, ground-state density, and laser field focused on a subwavelength scale. (b) Driven spin current density $j^s_{x,z}$ for different times during the pulse of duration T_p. (c) Evolution of first moment $\langle j^s_{x,z}\rangle_x$ in Eq. (14) during the application of the laser field.

$I^s_{xz}(t)$ is zero over the whole time since our vector beam cannot induce spatial imbalances into the electron wave functions. Moreover and related to it, it can be shown that $\langle x\rangle(t) \equiv 0$ (not shown for brevity). Surprisingly, even in equilibrium $I^s_{x,y} = -I^s_{y,x} \neq 0$, which is a consequence of the nonconservation of the electron spin in the presence of spin-orbit coupling [24].

In Figs. 3(b)–3(e) we present the time evolution of the spin current density $j^s_{x,z}$ for $\alpha_R = \alpha_0$ and the amplitude A_0, which belongs to the red curve in Fig. 2(a). Although the volume-integrated current is zero, the action of the azimuthal vector beam clearly initiates a nonzero current density with an oscillatory behavior. Further, the current density persists and keeps the oscillations in time once the light-matter interaction is off as presented by Fig. 3(d). The reason is the semioccupation of the ground and the excited states driving the spin polarization and therefore, the spin current back and forth.

For possible applications, the applied vector beam may take the role of a local spin (current) pump. For a demonstration of this effect, we enlarge the system size by a factor of 3, while focusing the beam down to a waist w_0 (distance intensity maximum to optical axis) of $\lambda/20$ ($\hbar\omega =$ 100 meV), as shown in Fig. 4(a). As a consequence, the spatially inhomogeneous vector potential component $A_y(x)$ is about the size of the ground-state width. The result is the excitation of very high states, $n \approx 60$, via the interaction Hamiltonian $\hat{H}_3(t)$, in the spectrum. The charge densities in these high semiclassical states peak near the classical turning points far away from the symmetry axis. The resulting effect on the light-driven spin current density is remarkable. In Fig. 4(b), we present the spatially dependent $j^s_{x,z}$ for different times during the laser application as received from our numerical propagation of the density matrix. The considered duration of the external light field amounts to 20 optical cycles, i.e., $T_p = 0.83$ ps. For short times ($t < 0.2T_p$, blue curve), the current density is strongly localized near the symmetry axis $x = 0$. However, at later times we see that the maximum of $j^s_{x,z}$ wanders to outer regions in the potential landscape, providing a clear proof that higher-lying states in the spectrum

are occupied. During the course of time, the spin current density oscillates in a known fashion and is characterized by an (spatially) odd function similar to Fig. 3. Interestingly, the major spin current dynamics happens at regions where the incident light wave is not present. See panel (c) of Fig. 4, where the corresponding first moment, defined as

$$\langle j^s_{x,z}\rangle_x = \int_{-\infty}^{\infty} dx\, x\big(j^s_{x,z}(x)\big), \tag{14}$$

is shown. The maximum increases drastically during the laser interaction and reaches distances of more than $4w_0$ to the symmetry axis. Further, due to the coherence of the laser field, the spin current density peaks for $x \lessgtr 0$ are strongly correlated. Hence, we demonstrated that the vector beam may act as a (local) spin current pump.

B. Elliptic 2D quantum dot structure

In a next step we reduce the confinement in y direction to $\Omega_y = 1.8\Omega_x$, meaning the transverse profile of the quantum dot takes the form of an ellipsis, as presented in panel (a) of Fig. 5. In contrast to the 1D case, $\boldsymbol{A}_{\mathrm{AVB}}(\boldsymbol{r}, t)\cdot\nabla \neq 0$, meaning $\hat{H}_1(t) = i(e\hbar/m^*)\boldsymbol{A}\cdot\nabla$ of the interaction Hamiltonian does not disappear.

The structured light field initiates quadrupole transitions, i.e., the Hamiltonian $\hat{H}_1(t)$, which conserves the spin orientation (with respect to projection on $|\uparrow,\downarrow\rangle$ of σ_z) and are also symmetry-conserving: an even (odd) wave function $\varphi_n^{\uparrow(\downarrow)}(\boldsymbol{r})$ couples with an even (odd) wave function $\varphi_{n'}^{\uparrow(\downarrow)}(\boldsymbol{r})$ via $\hat{H}_1(t)$. Consequently, the spin nonconserving Hamiltonian $\hat{H}_3(t) = e\alpha_R[\boldsymbol{A}(\boldsymbol{r}, t)\times\hat{\boldsymbol{\sigma}}]_z$ flips the spin orientation and couples an even (odd) wave function $\varphi_n^{\uparrow(\downarrow)}(\boldsymbol{r})$ with an odd (even) $\varphi_{n'}^{\downarrow(\uparrow)}(\boldsymbol{r})$ (see discussion in the 1D case).

To account for these symmetry conditions for the initial and target states, we set the laser field resonant to the lowest allowed (by first-order transitions) pair $|1\rangle$ and $|4\rangle$, which are characterized by the spin polarization numbers $\langle 1|\sigma_z|1\rangle = -0.92$ and $\langle 4|\sigma_z|4\rangle = 0.79$. As a consequence, we expect a partial flip of the total z component of the spin of the driven electron wave function due to the structured light-matter interaction.

Indeed, the temporal dependencies of the spin polarizations presented in Fig. 5(b) reveal such a spin-flip characterized by the transition $|\Psi_1\rangle \to |\Psi_4\rangle$. In the case of the z projection it stabilizes at a (time-averaged) value of 0.27 after laser excitation (field indicated by the gray, dashed curve). Interestingly, in comparison to the 1D case shown in Fig. 2, the additionally allowed dynamics in the y direction seem to boost the strength of this spin-flip. To complete the physical picture, we mention that the spin polarizations in x and y directions remain zero at any time. As above, we are in the perturbation regime where first-order processes dominate, as emphasized by the time-dependent occupation numbers in panel (c) of Fig. 5. The sum of the numbers $c_1 + c_4$ (green curve) is larger than 0.9 for the whole propagation time. Hence, only a small fraction of the initial wave function is splattered to higher states via multiphoton processes. In this vein, the sum $c_1 + c_4 + c_7$ (black curve), where $|7\rangle$ is accessible via two-photon transitions, is 0.99 after the light-matter interaction.

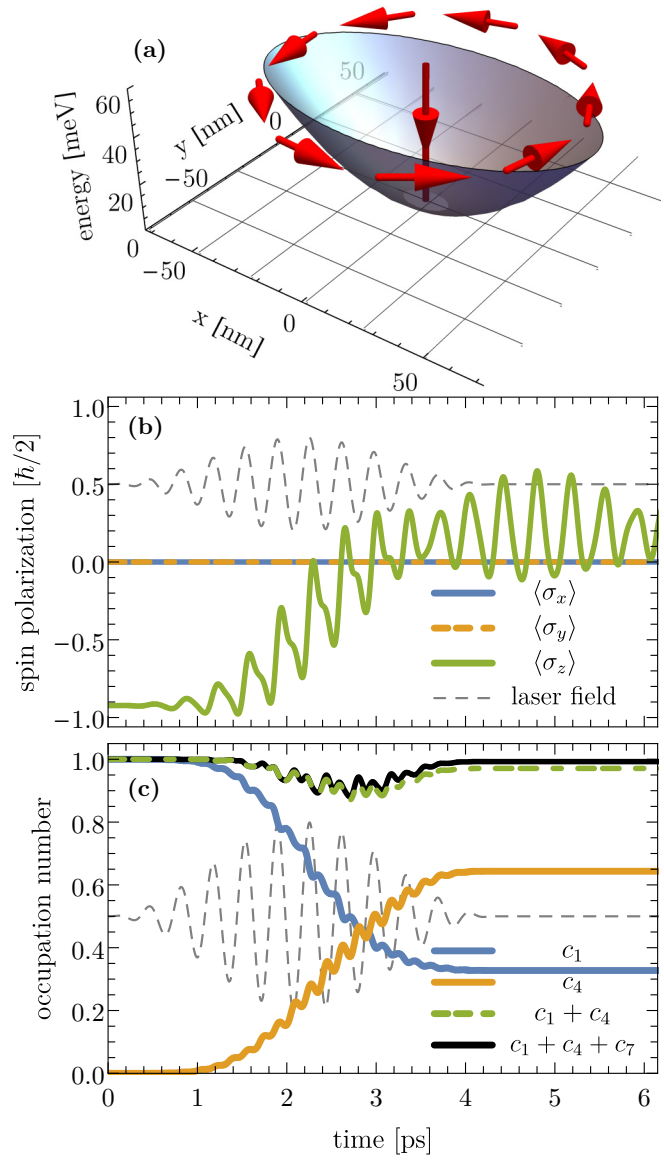

FIG. 5. (a) Geometry of the potential landscape and vector beam (indicated by red arrows). (b) Time-dependent spin polarization $\langle\Psi(t)|\sigma_i|\Psi(t)\rangle$ $i = x, y, z$ extracted from the propagation of the density matrix. The dotted gray line indicates the temporal profile of the RVB. (c) Time-dependent occupation numbers of the initial and target states $|1\rangle$ and $|4\rangle$, respectively. The green curve $c_1 + c_4$ is almost unity, indicating a single-photon process. Additionally, $c_1 + c_4 + c_7$ is shown where c_7 indicates access by a second-order process. All curves belong to the parameters $\alpha_R = \alpha_0$ and A_0.

It is interesting to study the transformation of the wave function under the action of the laser field in more detail. In Fig. 6(a), we present the projections of the time-dependent wave function (starting from $|\Psi_1\rangle$) onto the eigenstates of σ_z. For $t = 0$ (left panels), the spin-down projected wave function is much more pronounced than its counterpart, which corresponds to $\langle 1|\sigma_z|1\rangle = -0.92$. With time, the spin-up channel is more and more populated as a signature of the $|\Psi_1\rangle \to |\Psi_4\rangle$ transition. Further, we see transversal dynamics relative to the major axis of the potential ellipse due to the action of the azimuthal polarization of the incident light field (indicated by

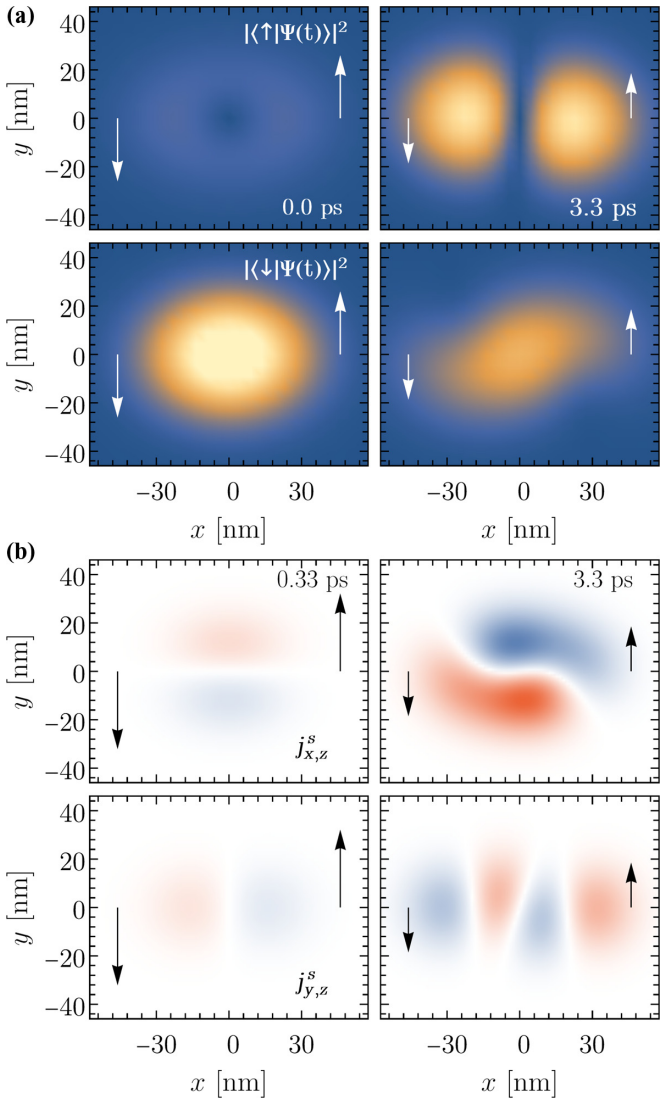

FIG. 6. (a) Time evolution of the wave function projected on eigenstates of σ_z during the laser propagation. The arrows mark direction of the local and temporal polarization direction. (b) Corresponding spin current densities $j_s^{x,z}$ and $j_s^{y,z}$. Blue (red) color marks here indicate negative (positive) sign. The system and laser parameters are the same as in Fig. 5.

the white arrows in the panel). Hence, the charge density is slightly pushed in the transverse (y) direction. However, in the whole propagation time frame, the position expectation values $\langle x\rangle(t)$ and $\langle y\rangle(t)$ are zero, which reflects the symmetry of the incident laser field. Another consequence is the absence of any volume-integrated charge current.

Similar to the 1D case, we do not find any volume-integrated spin current but only spin current densities with an odd spatial symmetry. In Fig. 6(b), we present the spin current densities $j^s_{x,z}$ and $j^s_{y,z}$ graphically. Already shortly after the pulse is switched on (left panels), spin currents emerge and oscillate in time (right panels), hence changing their local signs continuously. The reason is the partial occupation of the initial and final states, enabling spin dynamics with an oscillatory behavior.

C. Radially symmetric quantum dot

After inspecting a 2D structure with different confinement strengths in the x and y directions, we turn our interest to a radially symmetric quantum dot, i.e., $\hbar\Omega_x = \hbar\Omega_y$. In such a structure, the symmetry coincides with that of the intensity profile of both considered vector beam classes. Although both vector beam classes show the same intensity pattern, their physical action is entirely different. As shown in Ref. [18], the light-matter interaction with the RVB is strongly electric, while the AVB shows a strong magnetic-type interaction in cylindrical symmetry: the electric field component of the AVB is azimuthally directed, and thus, the coupling $\boldsymbol{E}_{\mathrm{AVB}} \cdot \boldsymbol{r}$ disappears in a radially symmetric quantum dot. Nevertheless, in a spin-active physical system, the electromagnetic vector potential provides an effective AVB-matter interaction via $\hat{H}_2(t)$ and $\hat{H}_3(t)$. A symmetry analysis reveals the same "selection rules" for the first-order transitions as in the former cases.

In Fig. 7 we present the electron dynamics for a system with a SOC strength $\alpha_R = 0.8\alpha_0$ and a ten-cycle laser field with amplitude of $0.75A_0$. The laser frequency is resonant with the next-higher-lying state corresponding to the allowed first-order transition. As in the previous examples, we see a direct response of the spin polarization (panel a) to the AVB-matter interaction, which is emphasized by the time-dependent occupation numbers shown in Fig. 7(b). The time-averaged spin polarization—again, over oscillations during the free propagation—after the pulse is off (and before sensible relaxation kicks in) is 0.05. The spin polarization of the initial state $|\Psi_1\rangle$ is -0.864, while the target state is characterized by $\langle\Psi_6|\sigma_z|\Psi_6\rangle = 0.663$. We chose the parameters on purpose to achieve a quasi-spin-unpolarized state, because in such a case the spin current density is highest in magnitude and persists after the laser pulse is switched off. In principle, other laser parameters enable a strongly pronounced spin-flip, meaning the electron transitions to a large portion into the final state $|\Psi_6\rangle$. Such a situation is shown in Fig. 7(c) where we slightly adjusted system and laser parameters. As presented by the time-dependent spin polarization, the transition $|\Psi_1\rangle \to |\Psi_6\rangle$ is much more pronounced, i.e., starting from $\langle\sigma_z\rangle = -0.72$, the polarization flips totally during the AVB-matter interaction. After the pulses are turned off, it stabilizes at a time-averaged value of 0.5, which is remarkable considering it is mainly due to first-order processes.

Let us investigate the time evolution of the charge and spin current densities for the laser parameters corresponding to a final spin-unpolarized state [cf. Figs. 7(a) and 7(b)] in detail, as presented in Fig. 8. The spin-projected charge densities corresponding to the interaction with the AVB represent nicely the polarization pattern of the vector beam, as the sum $|\langle\boldsymbol{r},\uparrow|\Psi(t)\rangle|^2 + |\langle\boldsymbol{r},\downarrow|\Psi(t)\rangle|^2$ is always radially symmetric. However, the individual projections are not necessarily radially symmetric, as a closer inspection of the right panels in Fig. 8(a) reveals. Consequently, on the spin-polarized level, the position-dependent polarization vector clearly breaks the cylindrical symmetry. As in the previous examples, the population of the eigenstates with positive spin polarization increases during the AVB-matter interaction, while the spin-down projection is decaying continuously. After the pulse is off, both projections are of equal intensity, which is in

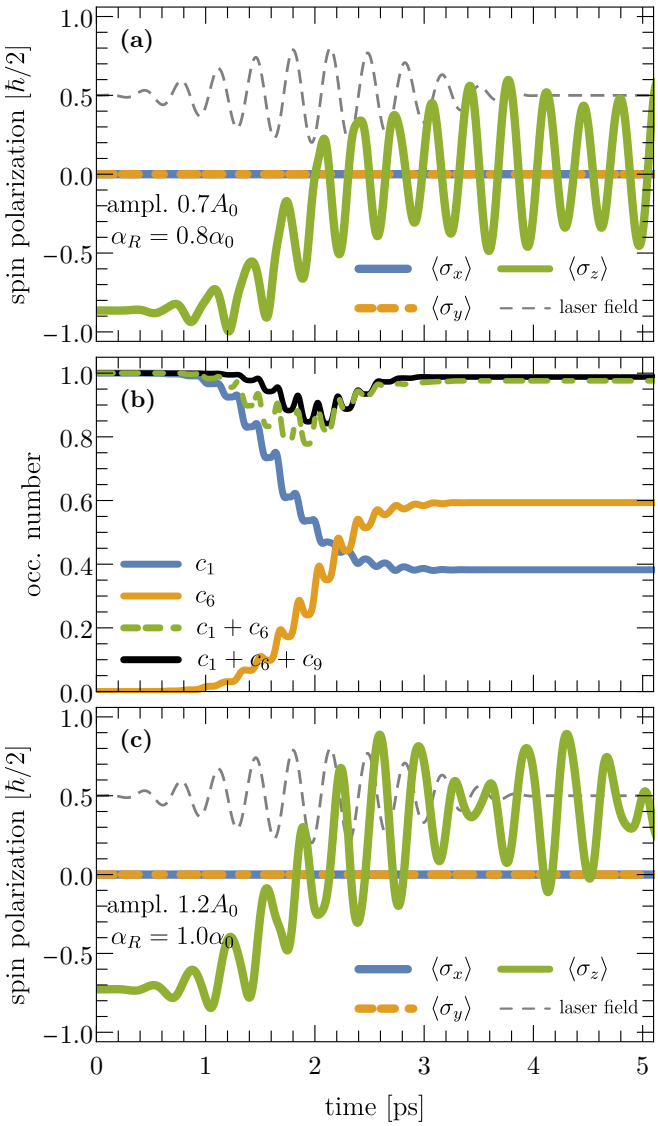

FIG. 7. Electron dynamics of a radially symmetric quantum dot irradiated by an azimuthal vector beam. (a) Time dependence of the spin polarizations in the three spatial directions. (b) Time-dependent occupation numbers. The system and field parameters are $\alpha_R = 0.8\alpha_0$ and $0.7A_0$ and $n_p = 10$ optical cycles. (c) Time dependence of the spin polarizations for $\alpha_R = \alpha_0$ and $1.2A_0$.

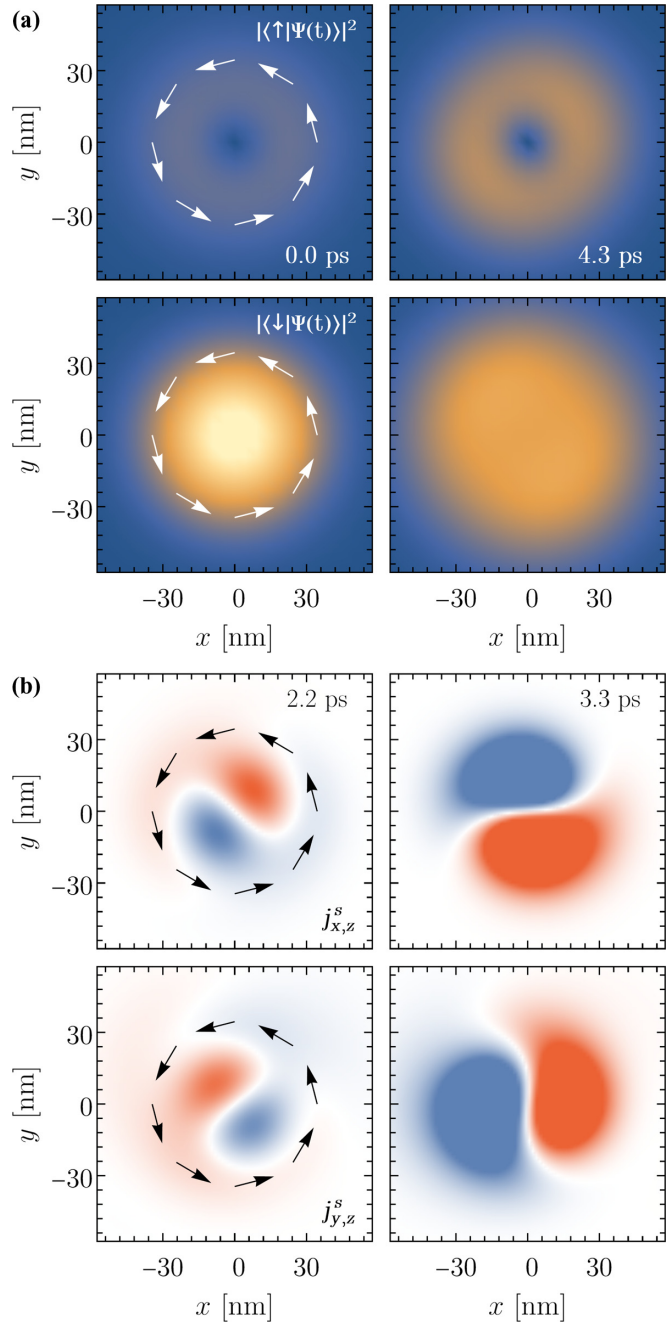

FIG. 8. Time evolution of the charge and spin current density initiated by an irradiated azimuthal vector beam: (a) spin-resolved charge densities and (b) spin current densities $j^s_{x,z}$ and $j^s_{y,z}$. Blue (red) color indicates a negative (positive) current. The system and laser parameters are the same as in Figs. 7(a) and 7(b).

accordance with Fig. 7(a), and the reason for the (final) spin unpolarized state for $t > 3$ ps.

The spin current densities show similar characteristics as in the former case: they present spatially odd functions, resulting in vanishing volume-integrated spin currents. The potential confinement allows two spin current densities, i.e., $j^s_{x,z}$ and $j^s_{y,z}$, which are shown in Fig. 8(b). The panels reveal interesting spatial structures with areas of highly positive and negative amplitude. As before, these structures are oscillating in time so that the local sign of density is changing continuously.

IV. CONCLUSIONS

We studied coupled electron spin and position dynamics induced by radially and azimuthally polarized cylindrical vector beams in one- and two-dimensional quantum dots of different symmetries. In general, this dynamics involving spin-position entangled electron states includes spin-flip transitions, changes in the orbital states, and, correspondingly, injection of spin currents. These processes strongly depend on the topology of the fields, being prohibited for the radial and allowed for the azimuthal vector beams. We analyzed the evolution of the orbital and spin degrees of freedom driven driven by the multicycle pulses of the azimuthal optical beams

and produced patterns of the spin density and the spin current tensors. These effects can be used for the design of the optical beams for spin manipulation in nanostructures of various geometries.

ACKNOWLEDGMENTS

E.Y.S. acknowledges support by the Spanish Ministry of Science, Innovation and Universities, and the European Regional Development Fund FEDER through Grant No. PGC2018-101355-B-I00 (MCIU/AEI/FEDER, UE) and the Basque Country Government through Grant No. IT986-16. J.W. acknowlegdes financial support from the Deutsche Forschungsgemeinschaft (DFG) through Grant No. WA 4352/2-1

APPENDIX

The electric and magnetic fields of the RVB are given by

$$\boldsymbol{E}_{\mathrm{RVB}}(\boldsymbol{r},t) = E_0\Big(J_1(q_\perp\rho)\sin(q_\parallel z-\omega t)\hat{\epsilon}_\rho + \frac{q_\perp}{q_\parallel}J_0(q_\perp\rho)\cos(q_\parallel z-\omega t)\hat{\epsilon}_z\Big), \tag{A1}$$

and

$$\boldsymbol{B}_{\mathrm{RVB}}(\boldsymbol{r},t) = A_0\frac{q^2}{q_\parallel}J_1(q_\perp\rho)\sin(q_\parallel z-\omega t)\hat{\epsilon}_\varphi, \tag{A2}$$

where $E_0 = A_0\omega$. Exploiting the localization of quantum structure, we can expand the Bessel functions into $J_1(x) \simeq x/2$ and $J_0(x) \simeq 1$. Building the Poincaré electromagnetic potentials yields

$$\begin{aligned}\boldsymbol{A}'_{\mathrm{RVB}}(\boldsymbol{r},t) = &-\frac{q_\perp q^2}{2q_\parallel^4 z^2}\rho\big[\big(q_z^2z^2-2\big)\cos(q_z z-\omega t)\\ &+2\cos(\omega t)-2q_z z\sin(q_\parallel z-\omega t)\big]\hat{\epsilon}_\rho\\ &+\frac{q_\perp q^2}{2q_\parallel^4 z^3}\rho^2\big[\big(q_z^2z^2-2\big)\cos(q_\parallel z-\omega t)\\ &+2\cos(\omega t)-2q_z z\sin(q_\parallel z-\omega t)\big]\hat{\epsilon}_z,\end{aligned} \tag{A3}$$

and

$$\begin{aligned}\Phi'_{\mathrm{RVB}}(\boldsymbol{r},t) = &\frac{E_0 q_\perp}{2q_\parallel^2 z^2}[q_z\rho^2 z\cos(q_\parallel z-\omega t)\\ &-(\rho^2+2z^2)(\sin(\omega t)+\sin(q_\parallel z-\omega t))].\end{aligned} \tag{A4}$$

In the transversal plane $z=0$ we obtain $\boldsymbol{A}'(\boldsymbol{r},t) = (q_\perp q^2/6q_\parallel)A_0\rho^2\Omega(t)\sin(\omega t)\hat{\epsilon}_z$ and $\Phi'_{\mathrm{RVB}}(\boldsymbol{r},t) = (E_0/4)q_\perp\rho^2\sin(\omega t)$.

The electric and magnetic fields of the AVB are given by

$$\boldsymbol{E}_{\mathrm{AVB}}(\boldsymbol{r},t) = E_0J_1(q_\perp\rho)\cos(q_\parallel z-\omega t)\hat{\epsilon}_\varphi \tag{A5}$$

and

$$\begin{aligned}\boldsymbol{B}_{\mathrm{AVB}}(\boldsymbol{r},t) = A_0(&-q_\parallel J_1(q_\perp\rho)\cos(q_\parallel z-\omega t)\hat{\epsilon}_\rho\\ &+q_\perp J_0(q_\perp\rho)\sin(q_\parallel z-\omega t)\hat{\epsilon}_z).\end{aligned} \tag{A6}$$

Building the Poincaré electromagnetic potentials yields, in the plane $z=0$,

$$\boldsymbol{A}'_{\mathrm{AVB}}(\boldsymbol{r},t) = -\tfrac{1}{2}q_\perp\rho\sin(\omega t)\hat{\epsilon}_\varphi, \tag{A7}$$

and

$$\Phi'_{\mathrm{AVB}}(\boldsymbol{r},t) = 0. \tag{A8}$$

[1] I. Žutić, J. Fabian, and S. Das Sarma, Rev. Mod. Phys. **76**, 323 (2004).

[2] M. M. Glazov, *Electron & Nuclear Spin Dynamics in Semiconductor Nanostructures*, Series on Semiconductor Science and Technology Vol. 23 (Oxford University Press, Oxford, England, 2018).

[3] E. I. Rashba, Sov. Phys. -Solid State **2**, 1109 (1960).

[4] E. I. Rashba and Al. L. Efros, Phys. Rev. Lett. **91**, 126405 (2003).

[5] K. C. Nowack, F. H. L. Koppens, Y. V. Nazarov, and L. M. K. Vandersypen, Science **318**, 1430 (2007).

[6] Y. Tokura, W. G. van der Wiel, T. Obata, and S. Tarucha, Phys. Rev. Lett. **96**, 047202 (2006).

[7] E. A. Laird, C. Barthel, E. I. Rashba, C. M. Marcus, E. A. Hanson, and A. C. Gossard, Semicond. Sci. Technol. **24**, 064004 (2009).

[8] *Spin Physics in Semiconductors*, edited by M. I. Dyakonov, Springer Series in Solid-State Sciences (Springer, New York, 2008).

[9] M. J. Stevens, A. L. Smirl, R. D. R. Bhat, A. Najmaie, J. E. Sipe, and H. M. van Driel, Phys. Rev. Lett. **90**, 136603 (2003).

[10] R. D. R. Bhat, F. Nastos, A. Najmaie, and J. E. Sipe, Phys. Rev. Lett. **94**, 096603 (2005).

[11] A. Najmaie, E. Ya. Sherman, and J. E. Sipe, Phys. Rev. Lett. **95**, 056601 (2005).

[12] L. Allen, M. W. Beijersbergen, R. J. C. Spreeuw, and J. P. Woerdman, Phys. Rev. A **45**, 8185 (1992).

[13] K. Volke-Sepulveda, V. Garcés-Chávez, S. Chávez-Cerda, J. Arlt, and K. Dholakia, J. Opt. B: Quantum Semiclass. Opt. **4**, S82 (2002).

[14] Q. Zhan, Adv. Opt. Photon. **1**, 1 (2009).

[15] M. Veysi, C. Guclu, and F. Capolino, J. Opt. Soc. Am. B **32**, 345 (2015).

[16] R. Dorn, S. Quabis, and G. Leuchs, Phys. Rev. Lett. **91**, 233901 (2003).

[17] G. Volpe and D. Petrov, Opt. Commun. **237**, 89 (2004).

[18] J. Wätzel, C. M. Granados-Castro, and J. Berakdar, Phys. Rev. B **99**, 085425 (2019).

[19] S. Vyas, Y. Kozawa, and S. Sato, Opt. Expr. **21**, 8972 (2013).
[20] C. Tannoudji, G. Grynberg, and J. Dupont-Roe, *Atom-Photon Interactions* (John Wiley and Sons Inc., New York, 1992).
[21] S. Nadj-Perge, S. M. Frolov, E. P. A. M. Bakkers, and L. P. Kouwenhoven, Nature (London) **468**, 1084 (2010).
[22] J. Takeda, K. Yoshioka, Y. Minami, and I. Katayama, J. Phys. D **51**, 103001 (2018).
[23] Q.-F. Sun and X. C. Xie, Phys. Rev. B **72**, 245305 (2005).
[24] E. I. Rashba, Phys. Rev. B **68**, 241315(R) (2003).